

## Article

# Tensile Deformation Behavior of a Directionally Solidified Superalloy at Cryogenic Temperatures

Xiaotong Guo <sup>1,2,†</sup>, Yiqiang Ni <sup>2,†</sup>, Ganqiang Wang <sup>3</sup>, Zeshan Liang <sup>1</sup>, Hemeng Peng <sup>1</sup>, Xiaofeng Yang <sup>2</sup> and Zhiwei Fu <sup>2,\*</sup>

<sup>1</sup> Chongqing CEPREI Industrial Technology Research Institute Co., Ltd., Chongqing 401332, China; guoxiaotong0713@163.com (X.G.); liangzeshan@ceppei.com (Z.L.); penghemeng@ceppei.biz (H.P.)

<sup>2</sup> China Electronic Product Reliability and Environmental Testing Research Institute, Guangzhou 511370, China; niyiqiang@ceppei.com (Y.N.); yangxiaofeng@ceppei.com (X.Y.)

<sup>3</sup> Beijing CESI Technology Co., Ltd., Beijing 100176, China; 18811016732@163.com

\* Correspondence: fzw19940124@163.com; Tel.: +20-87-234-023

† These authors contributed equally to this work.

**Abstract:** Ni-based superalloys are widely used to manufacture gas turbine core components, but reports on the reliability of superalloys at cryogenic temperatures are still limited. Considering the actual application of superalloys in the field of cryogenic temperature, the tensile deformation behavior of directionally solidified superalloy DZ406 was investigated at cryogenic temperatures from  $-125\text{ }^{\circ}\text{C}$  to  $25\text{ }^{\circ}\text{C}$ , and the comparative analysis of room temperature and  $1000\text{ }^{\circ}\text{C}$  was carried out. The yield strength and ultimate strength at cryogenic temperatures were close to that at room temperature, and twice that at  $1000\text{ }^{\circ}\text{C}$ . The elongation was maintained at 10–15% and exhibited a certain plasticity at cryogenic temperatures. The morphologies and chemical composition of  $\gamma'$  precipitates were close at cryogenic temperatures, room temperature and  $1000\text{ }^{\circ}\text{C}$ . The microstructure difference that was caused by different temperatures was mainly reflected in the fracture mode and dislocation configuration. At cryogenic temperature, the fracture samples basically exhibited no necking phenomenon, and the cracks were basically located in the interdendritic regions and occurred in MC carbide itself; at room temperature and  $1000\text{ }^{\circ}\text{C}$ , dimples with carbides inside were distributed on the fracture surface. Slip bands and dislocations contributed to the tensile deformation at cryogenic temperatures and room temperature, while only the dislocations worked at  $1000\text{ }^{\circ}\text{C}$ .

**Keywords:** superalloy; tensile property; cryogenic temperature; microstructure; dislocation



**Citation:** Guo, X.; Ni, Y.; Wang, G.; Liang, Z.; Peng, H.; Yang, X.; Fu, Z. Tensile Deformation Behavior of a Directionally Solidified Superalloy at Cryogenic Temperatures. *Crystals* **2022**, *12*, 886. <https://doi.org/10.3390/cryst12070886>

Academic Editors: Chenglin Li, Nan Li and Pavel Lukáč

Received: 31 May 2022

Accepted: 16 June 2022

Published: 22 June 2022

**Publisher's Note:** MDPI stays neutral with regard to jurisdictional claims in published maps and institutional affiliations.



**Copyright:** © 2022 by the authors. Licensee MDPI, Basel, Switzerland. This article is an open access article distributed under the terms and conditions of the Creative Commons Attribution (CC BY) license (<https://creativecommons.org/licenses/by/4.0/>).

## 1. Introduction

Ni-based superalloys are favored for their excellent mechanical properties, corrosion resistance and long-term stability [1,2]. Thus, they are widely used to manufacture aero-engine and gas turbine core components, the service environment of which is among the worst service conditions. The production technology of Ni-based superalloys has experienced four typical development stages: forging, equiaxed grain casting, directional solidified casting and single crystal casting [3,4]. Generally, the higher the processing stage, the greater the processing difficulty and the better the properties of the alloy [4,5]. So far, most published research on the mechanical properties of Ni-based alloys focuses on the room temperature and high temperature range [6–11].

In the field of cryogenic applications, superalloys are the key materials for rocket engine turbopumps and some cryogenic pressure vessels. For example, China has developed forging GH4586, equiaxed casting K4169 and K4202 superalloys for the production of key components in a new generation liquid hydrogen and liquid oxygen rocket engine. However, the application potential of directionally solidified and single crystal superalloys at cryogenic temperature still needs to be developed. Meanwhile, in a low temperature service environment the boiling point of liquid oxygen reaches  $-183\text{ }^{\circ}\text{C}$ , posing a serious

threat to the safe service of the applied superalloys. The published reports on the cryogenic temperature reliability of Ni-base alloys mainly focus on forged alloys, such as the Haynes 282 alloy [12], alloy 625 [13], and GH3536 (Hastelloy X) [14]. The microstructure of the above forging alloys is relatively simple in comparison with casting superalloys, and the published studies mainly focus on the distribution of grains and micro-deformation mechanisms, such as stacking faults and dislocations [12–14]. However, the effect of typical microstructures of superalloys, such as carbides and grain boundaries on the tensile property at cryogenic temperature is still unclear.

The DZ406 superalloy is a directionally solidified Ni-based superalloy with 3 wt% Re in composition [3], and its comprehensive properties are equivalent to those of the first-generation Ni-based single-crystal superalloy. At present, the DZ406 superalloy has become one of the most promising directional solidification alloys in China. In this study, we conducted tensile tests of the DZ406 alloy at cryogenic temperatures and carried out the comparative tests at room temperature and high temperature. Through systematic characterization, including macroscopic fracture, microstructure morphologies and dislocation configurations, the tensile deformation behavior of DZ406 superalloy at cryogenic temperatures was finally revealed.

## 2. Materials and Methods

The as-received material was directionally solidified in a vacuum and cast into solid cylindrical bars by the Beijing Institute of Aeronautical Materials. The DZ406 superalloy cylindrical bars used in this study were columnar grains that were aligned along the  $\langle 001 \rangle$  orientation with a deviation within  $10^\circ$ . The standard solution treatment of DZ406 superalloy is:  $1275^\circ\text{C}/30\text{ min} + 1120^\circ\text{C}/4\text{ h} + 1180^\circ\text{C}/4\text{ h} + 870^\circ\text{C}/16\text{ h}$  (air cooling) [3], and all the experimental samples had experienced the standard solution treatment. The chemical composition of DZ406 superalloy was (in wt.%) 11.98 Co-6.77 Cr-6.28 Ta-6.02 Al-4.84 W-2.92 Re-1.53 Mo-1.48 Hf-0.12 C with a balance of Ni.

The tensile tests conducted at  $-125^\circ\text{C}$ ,  $-75^\circ\text{C}$ ,  $-25^\circ\text{C}$ ,  $25^\circ\text{C}$  (room temperature) were according to GB/T 228.1-2021, and the tests conducted at  $1000^\circ\text{C}$  were according to GB/T 228.2-2015. During the testing process, the tensile force was applied when the tensile temperature was kept stable for 20 min. The tensile rate was maintained at  $1 \times 10^{-3}\text{ s}^{-1}$  during the whole testing process. The diameter and length of the gauge area of the cylindrical tensile specimens was 5 mm and 25 mm, respectively. The axial direction of all the tensile specimens was consistent with the  $\langle 001 \rangle$  direction of raw cylindrical bars. Two to three specimens were tested for each condition for statistical significance.

To observe the microstructures and/or dislocation configurations at the cross section after standard heat treatment and tensile fracture, the specimens were cut along the direction that was perpendicular to  $\langle 001 \rangle$ . To observe the microstructure of the longitudinal section of the alloy after tensile fracture, the specimens were cut along the direction that was parallel to  $\langle 001 \rangle$ . The samples were ground and eroded for microstructure characterization using the standard metallographic techniques. A solution containing 5 g of copper sulfate, 1.25 mL of sulfuric acid, 25 mL of hydrochloric acid and 20 mL of water was employed to etch the samples. A NIKON LV150 optical microscope, ZEISS SUPRA 55 and a FEI Inspect F50 field-emission scanning electron microscope (FE-SEM) were used to observe the microstructures. For the dislocation observation, the 3 mm disks sectioned from the fractured samples were grinded to 50–60  $\mu\text{m}$  and then electrochemically thinned in a twin-jet polished machine in a solution of 10 vol% perchloric acid and 90 vol% ethanol. A FEI Talos F200X TEM was used to observe the dislocations, and the compositions of the  $\gamma$  matrix and  $\gamma'$  precipitates were measured using the high-angle annular dark field (HAADF) detector through the STEM-EDX mode.

### 3. Results and Discussion

#### 3.1. As-Received Microstructure

Figure 1 shows the as-received microstructure of the DZ406 superalloy at the cross sections after the standard solution treatment. Carbides and  $\gamma/\gamma'$  eutectic were distributed in the interdendritic regions, and the microstructures of the dendrite core regions were relatively simple (Figure 1a). A higher magnification SEM image in Figure 1b shows that cuboidal  $\gamma'$  particles precipitated in the dendrite core regions, and the area fraction of the  $\gamma'$  precipitates was 66.2%. Moreover, small  $\gamma'$  particles were also observed in the  $\gamma$  channel and were generally precipitated from the  $\gamma$  matrix during the cooling process after the standard solution treatment. Figure 1c depicts the morphology of the interdendritic regions where sunflower-like  $\gamma/\gamma'$  eutectic and carbides were distributed. As the DZ406 superalloy contains MC carbide-forming elements Nb, Ti, Ta and Hf, there are two types of MC carbides after the standard solution treatment; one is a script-like and fine granular  $MC_{(1)}$  that is rich in Ti and Nb elements, and the other is a large granular  $MC_{(2)}$  that is rich in Ta and Hf elements. The distribution characteristics of MC carbides were consistent with other Ni-based superalloys that were enriched in Hf [11]. Similar to the interdendritic regions, the  $MC_{(1)}$  and  $MC_{(2)}$  carbides were also distributed in the grain boundary, as shown in Figure 1d.

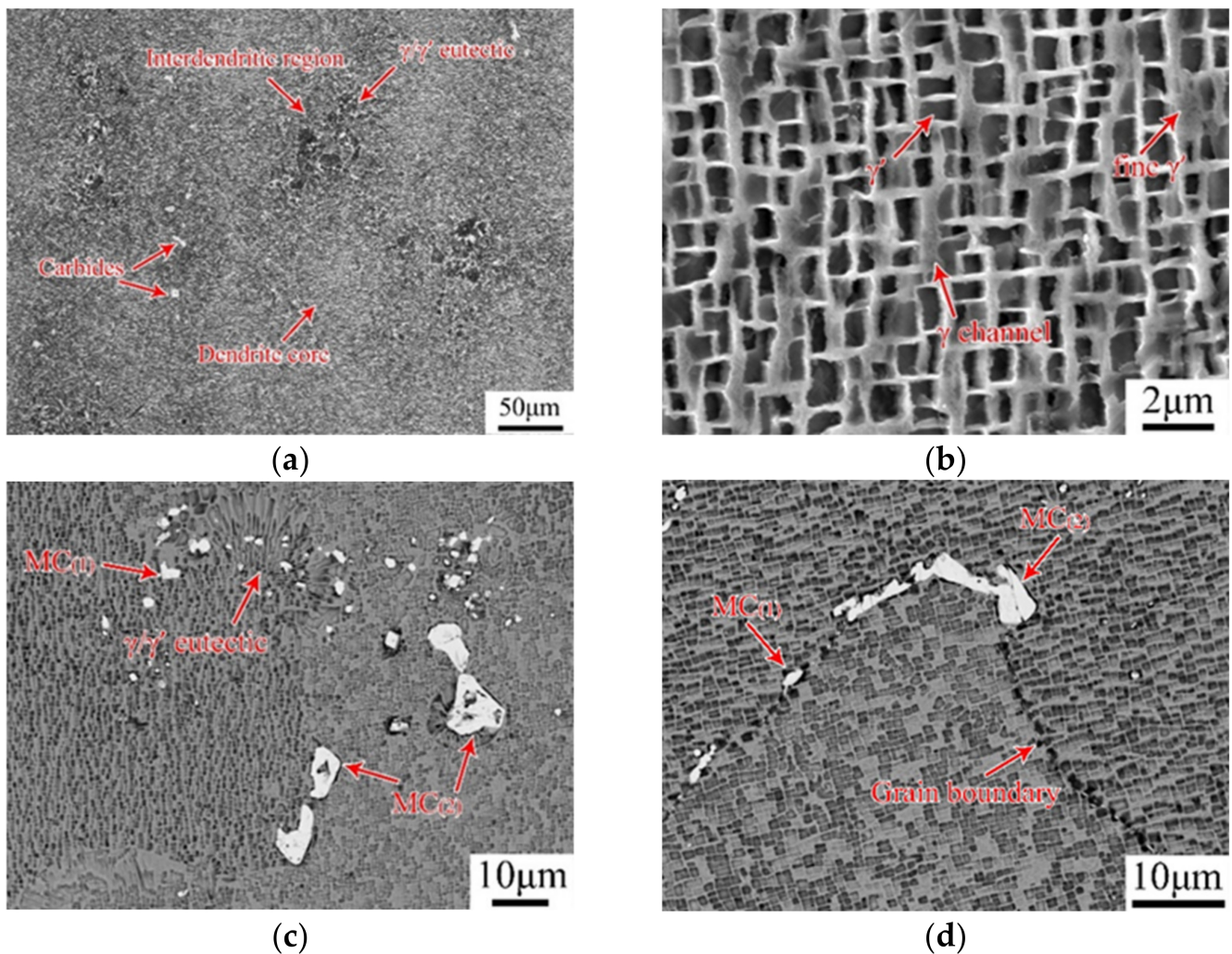


**Figure 1.** As-received microstructure of DZ406 superalloy at the cross sections after the standard solution treatment: (a) optical microstructure; (b) SEM-SE image of  $\gamma'$  precipitates in the dendrite core region; (c) SEM-BSE image of interdendritic carbides; (d) SEM-BSE image of grain boundary.

### 3.2. Tensile Properties at Cryogenic Temperatures

To explore the tensile properties of the DZ406 superalloy at cryogenic temperatures, tensile tests were conducted at  $-125\text{ }^{\circ}\text{C}$ ,  $-75\text{ }^{\circ}\text{C}$  and  $-25\text{ }^{\circ}\text{C}$ , respectively. The detailed tensile property parameters are listed in Table 1. The yield strength and ultimate strength of the DZ406 superalloy remained around 930 MPa and 1240 MPa and was basically unchanged in the cryogenic temperature range from  $-125\text{ }^{\circ}\text{C}$  to  $-25\text{ }^{\circ}\text{C}$ . The elongation of the alloy remained higher than 10% at cryogenic temperatures. At the same time, tensile tests were also carried out at room temperature and a high temperature of  $1000\text{ }^{\circ}\text{C}$  to better evaluate the tensile property at cryogenic temperatures. The tensile property of the DZ406 superalloy at room temperature was close to those at cryogenic temperatures, while the yield strength and tensile strength at cryogenic and room temperatures were significantly higher than those at  $1000\text{ }^{\circ}\text{C}$ . However, the elongation of the alloy at  $1000\text{ }^{\circ}\text{C}$  was 25.1%, which was about twice that at room temperature and at  $-125\text{ }^{\circ}\text{C}$ . Considering that the tensile properties of the alloy were basically unchanged in the temperature range of  $-125\text{ }^{\circ}\text{C}$  and  $-25\text{ }^{\circ}\text{C}$ , the following macro and micro analysis mainly focused on  $-125\text{ }^{\circ}\text{C}$ , room temperature and  $1000\text{ }^{\circ}\text{C}$  in this work.

**Table 1.** Yield strength, ultimate strength and elongation parameters of DZ406 superalloy in the temperature of  $-125\text{ }^{\circ}\text{C}$ ~ $1000\text{ }^{\circ}\text{C}$ .

Temperature ( $^{\circ}\text{C}$ )	Yield Strength (MPa)	Ultimate Strength (MPa)	Elongation (%)
$-125$	$936.3 \pm 10.7$	$1233.3 \pm 38.5$	$14.2 \pm 3.3$
$-75$	$924.0 \pm 12.5$	$1245.0 \pm 25.0$	$15.4 \pm 2.5$
$-25$	$928.0 \pm 14.1$	$1258.5 \pm 21.9$	$11.0 \pm 1.4$
25 (room temperature)	$910.5 \pm 9.2$	$1185.0 \pm 52.3$	$14.1 \pm 1.8$
1000	$423.5 \pm 4.9$	$581.0 \pm 7.8$	$25.1 \pm 3.5$

### 3.3. Macroscopic Fracture

The fracture morphologies experienced a systematic observation, and Figure 2 contains SEM images showing the fracture morphologies of the DZ406 superalloy tested at  $-125\text{ }^{\circ}\text{C}$ ,  $25\text{ }^{\circ}\text{C}$  and  $1000\text{ }^{\circ}\text{C}$ . At  $-125\text{ }^{\circ}\text{C}$ , the fracture specimens basically exhibited no necking phenomenon and a large number of secondary cracks and holes were observed on the fracture surface (Figure 2a). The macroscopic fracture did not show the typical plastic deformation characteristics, which was inconsistent with the elongation of more than 10% of the tensile samples. An enlarged image shows that a large number of carbides were cracked (Figure 2d), suggesting that as a kind of brittle phase, carbides were hard to deform and more prone to crack in the process of cryogenic temperature tensile. Due to the larger size of the  $\text{MC}_{(2)}$  carbides in comparison with the  $\text{MC}_{(1)}$  carbides, it was easier to accumulate stress and cracks inside of the  $\text{MC}_{(2)}$  carbides in the tensile process. Therefore, the cracking phenomenon of the  $\text{MC}_{(2)}$  carbides was more serious than that of the  $\text{MC}_{(1)}$  carbides.

The fracture mechanism of the DZ406 alloy was completely different at room temperature and  $1000\text{ }^{\circ}\text{C}$ , as shown in Figure 2b,c,e,f. Slight necking occurred when the alloy was tested at room temperature and  $1000\text{ }^{\circ}\text{C}$  (Figure 2b,c), resulting in a fracture surface area slightly smaller than that at  $-125\text{ }^{\circ}\text{C}$  (Figure 2a). The enlarged images of the fracture morphologies in Figure 2e,f further determined the mode of plastic fracture at above  $0\text{ }^{\circ}\text{C}$ . Numerous dimples were found on the fracture surface at room temperature and  $1000\text{ }^{\circ}\text{C}$ , and carbides could be observed in the middle of the dimples. This phenomenon indicates that the DZ406 superalloy presents obvious plastic deformation in the tensile process, and the stress concentration occurs easily at the interface between carbides and the  $\gamma$  matrix. It is worth noting that this high temperature deformation mechanism is generally accepted for the DZ406 alloy, for example, the creep voids are all located at the interfaces of the MC carbides and  $\gamma$  matrix during high temperature creep [15]. Generally, the dimples are nucleated, grown,

aggregated and finally connected with each other, resulting in plastic fracture [16,17]. The carbides with a smaller size were more conducive to the generation of dimples, as shown in the Figure 2e,f.

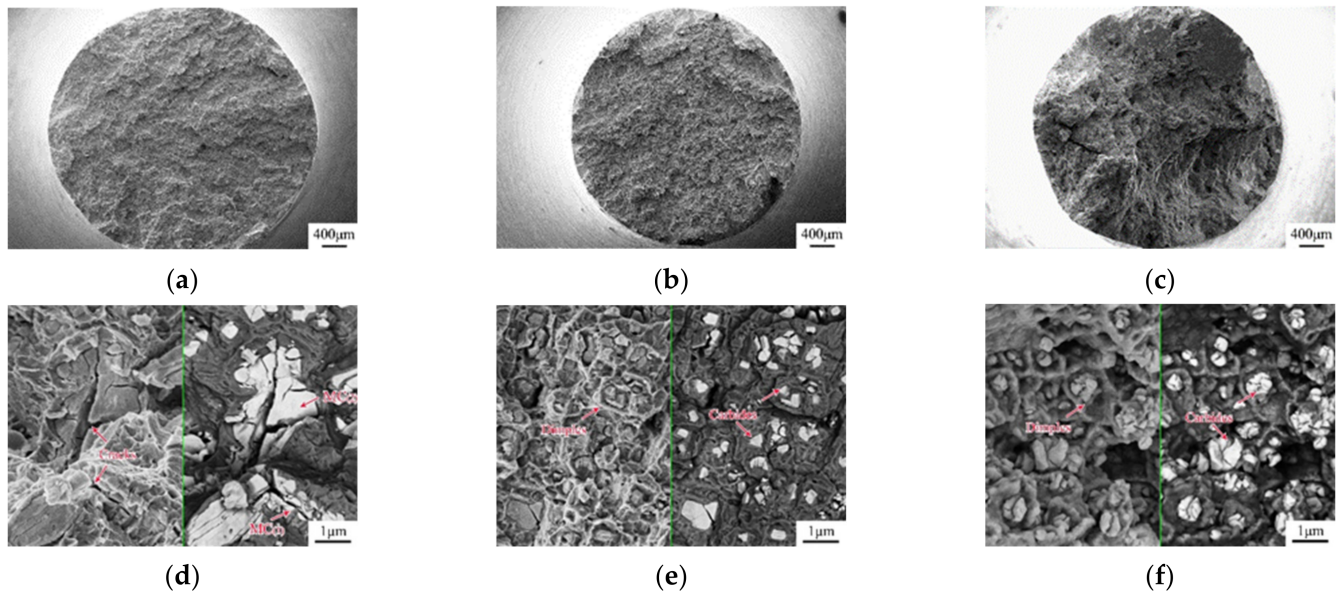


**Figure 2.** SEM images of fracture morphologies of DZ406 superalloy at a lower and higher magnification when tested at  $-125\text{ }^{\circ}\text{C}$  (a,d),  $25\text{ }^{\circ}\text{C}$  (b,e) and  $1000\text{ }^{\circ}\text{C}$  (c,f).

The fracture microstructures at the longitudinal sections were further observed to confirm the characteristics of tensile cracks distribution. Figure 3 are SEM-BSE images of a fracture microstructure at the longitudinal sections close to the fracture surface of DZ406 superalloy. The difference of thermal expansion between carbides and  $\gamma$  matrix lead to the stress concentration and interface cracking [18]. The tensile cracks were located at the interfaces of the carbides and  $\gamma$  matrix at  $-125\text{ }^{\circ}\text{C}$  and room temperature, while the carbides suffered self-cracking at  $-125\text{ }^{\circ}\text{C}$ , as shown in Figure 3a,b. However, a large number of cracks were found in the grain boundaries beside the interdendritic regions when tested at  $1000\text{ }^{\circ}\text{C}$  (Figure 3c,d). The above phenomenon showed that when the tensile temperature increased to  $1000\text{ }^{\circ}\text{C}$ , the strength of the grain boundary decreased, making both the interdendritic region and the grain boundary weak areas that are prone to initiating cracks. The grain boundary in Ni-based alloys plays a strengthening role at room temperature and low temperature, while it often becomes a weak region at high temperature [16]. For metal materials, the grain boundary strength is higher than that in the grain below the critical temperature, but the result is opposite above the critical temperature [16]. The fracture microstructures show that the critical temperature of the DZ406 alloy is between room temperature and  $1000\text{ }^{\circ}\text{C}$ , which leads to the fracture region of the DZ406 alloy located in the interdendritic region at room temperature and cryogenic temperature, while in both the grain boundary and interdendritic region at  $1000\text{ }^{\circ}\text{C}$ .

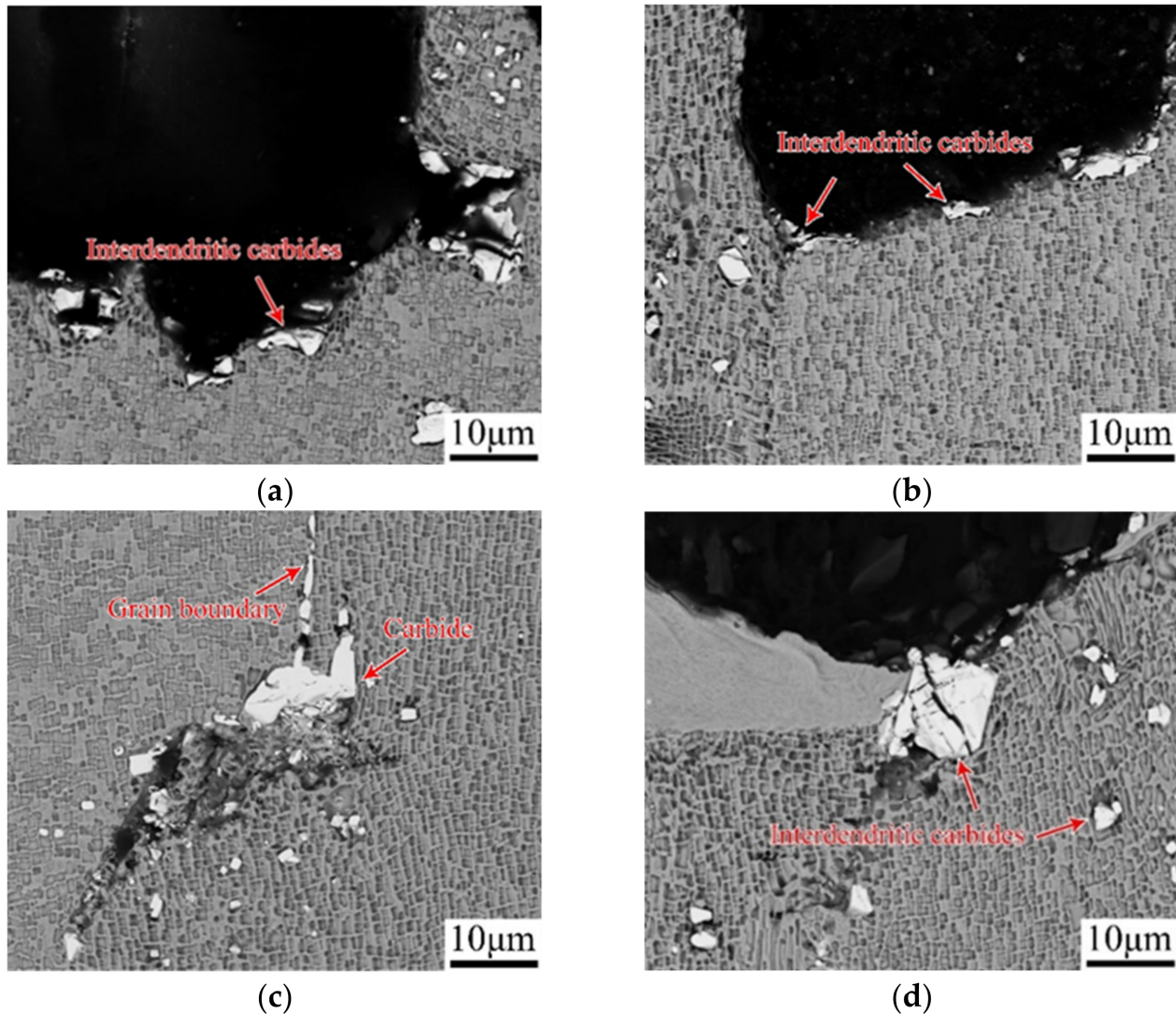


**Figure 3.** SEM-BSE images of fracture microstructure at the longitudinal sections close to the fracture surface of DZ406 superalloy when tested at  $-125\text{ }^{\circ}\text{C}$  (a),  $25\text{ }^{\circ}\text{C}$  (b),  $1000\text{ }^{\circ}\text{C}$  (c) and (d).

#### 3.4. Strengthening $\gamma'$ Phase Response

As the main reinforcing phase in cast Ni-based superalloys, the area fraction, distribution and size, and composition characterization of  $\gamma'$  phase are crucial to the tensile property [8,15,18]. Thus, the microstructures of the  $\gamma'$  precipitates were systematically characterized and quantified in the tensile samples. The SEM-SE images in Figure 4 show the morphologies of  $\gamma'$  precipitates in the dendrite core regions at the longitudinal sections close to the fracture surface of the tensile rupture specimens of the DZ406 superalloy. Figure 4a,b show the morphologies of  $\gamma'$  precipitates at a tensile temperature of  $-125\text{ }^{\circ}\text{C}$  at a low magnification and high magnification, respectively. The  $\gamma'$  phase maintained a good cuboidal morphology and fine  $\gamma'$  particles still existed in the  $\gamma$  channel. The morphology of the  $\gamma'$  phase was basically consistent with that after the standard solution treatment. At room temperature, the morphology of the  $\gamma'$  phase was basically consistent with that at  $-125\text{ }^{\circ}\text{C}$ , as shown in Figure 4c. When the temperature rose to  $1000\text{ }^{\circ}\text{C}$ , the  $\gamma'$  phase still basically maintained a cuboidal shape, but due to the relatively high tensile temperature, the small  $\gamma'$  particles in the  $\gamma$  channel dissolved (Figure 4d). Overall, due to the low testing temperature and short duration of the tensile testing process, microstructural degradation of the  $\gamma'$  precipitates was basically negligible.

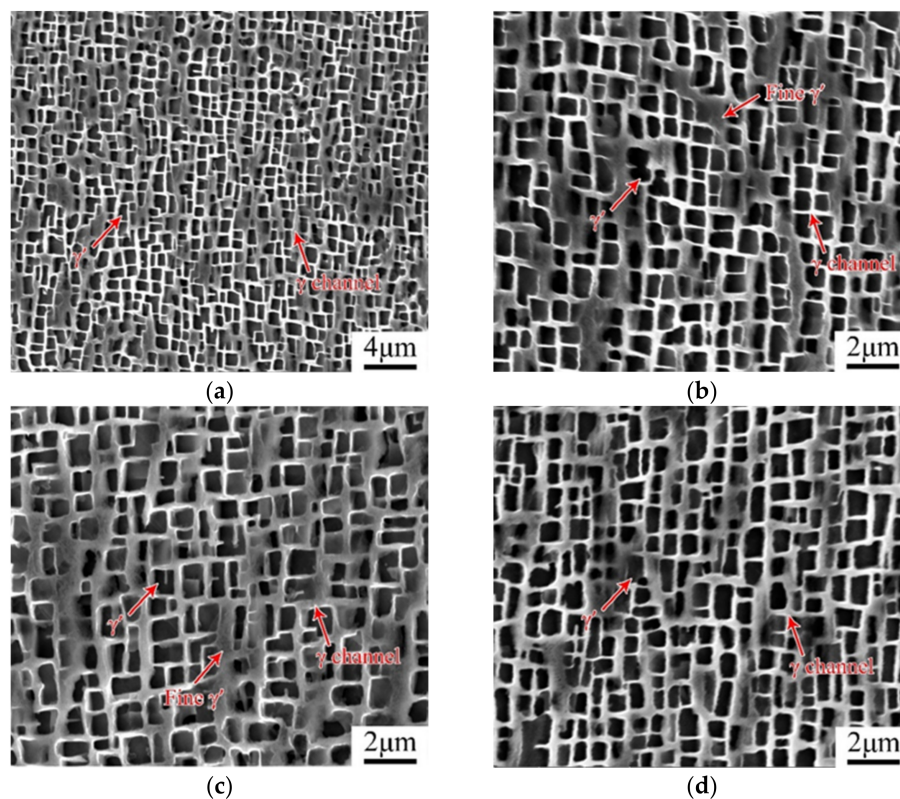


**Figure 4.** SEM-SE images of  $\gamma'$  precipitates in the dendrite core regions at the longitudinal sections close to the fracture surface of tensile rupture specimens of DZ406 superalloy: a lower magnification (a) and a higher magnification at  $-125\text{ }^{\circ}\text{C}$  (b),  $25\text{ }^{\circ}\text{C}$  (c) and  $1000\text{ }^{\circ}\text{C}$  (d).

Element distribution between  $\gamma$  and  $\gamma'$  phases is important to the strengthening effect of  $\gamma'$  precipitates [19–21], thus the chemical compositions of the above two phases were measured using STEM-EDX at different testing temperatures. Figure 5 depicts the element mapping of the  $\gamma$  matrix and  $\gamma'$  precipitates in the cross sections that are close to the fracture surface of the DZ406 superalloy tested at  $-125\text{ }^{\circ}\text{C}$ . The  $\gamma$  phase was enriched in Co, Cr and Re, while the  $\gamma'$  phase was enriched in Ni, Al, W and Ta. It is worth noting that the composition characteristics of  $\gamma$  and  $\gamma'$  phases were consistent at  $-125\text{ }^{\circ}\text{C}$ , room temperature and  $1000\text{ }^{\circ}\text{C}$ .

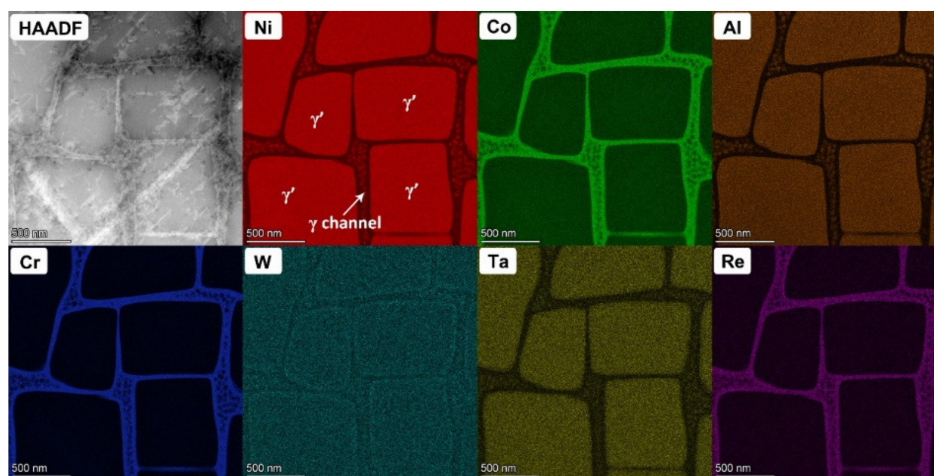


**Figure 5.** Element mapping of  $\gamma$  matrix and  $\gamma'$  precipitates in the dendrite cores at the cross sections close to the fracture surface of DZ406 superalloy tested at  $-125\text{ }^{\circ}\text{C}$ .

Figure 6a,b show the measured compositions of the  $\gamma$  matrix and  $\gamma'$  phase in the dendrite cores at the cross sections that are close to the fracture surface of the DZ406 superalloy. The chemical compositions of the  $\gamma$  phase and  $\gamma'$  phase were similar at all the testing conditions. The  $\gamma$  phase mainly included 50% Ni, 20% Co, 18% Cr and 5% Al, and the  $\gamma'$  phase mainly included 68% Ni, 13% Al and 9% Co (in at. %). Other elements, including W, Mo, Hf, Ta and Re, also exhibited segregation behavior, but the content in the  $\gamma$  and  $\gamma'$  phases was low due to the low content of alloy compositions. The element segregation  $k'$  between the  $\gamma$  matrix and  $\gamma'$  phase was calculated, and a  $k'$  value larger than 1 indicates segregation to  $\gamma$  matrix, while a value lower than 1 indicates segregation to the  $\gamma'$  phase. Figure 6c depicts the element segregation  $k'$  between the  $\gamma$  matrix and  $\gamma'$  phase, and no obvious differences in element segregation at different tensile temperatures was observed. The compositions of the  $\gamma$  matrix and  $\gamma'$  phase seemed not affected by external heat and stress, such as creep/tensile under certain conditions, as we found before in DZ406 and K465 superalloys [15,22].

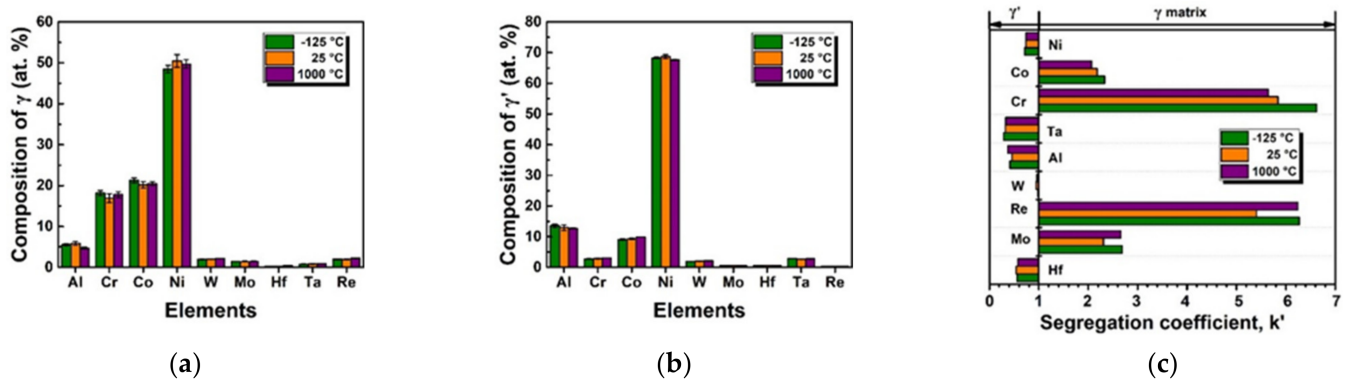


**Figure 6.** Measured compositions of  $\gamma$  matrix (a) and  $\gamma'$  phase (b), and element segregation coefficient between  $\gamma'$  and  $\gamma$  phases (c) in the dendrite cores at the cross sections close to the fracture surface of DZ406 superalloy tested at  $-125$  °C,  $25$  °C and  $1000$  °C using STEM-EDX (at. %).

Our results identified that the morphology of the secondary  $\gamma'$  phase was close to that after the standard solution treatment (Figures 1b and 4), and still basically retained a cuboidal morphology. Moreover, the compositions of the  $\gamma$  and secondary  $\gamma'$  phases were also similar at  $-125$  °C,  $25$  °C and  $1000$  °C (Figures 5 and 6). This means that the effect of the microstructure parameters that we normally pay attention to, including area fraction, size and distribution of secondary  $\gamma'$  precipitates can be ignored when considering the tensile properties of the DZ406 superalloy in a wide range. However, it should be noted that the microscopic dislocation configurations may be different under different tensile conditions, resulting in a different enhancement mechanism of the  $\gamma'$  phase.

### 3.5. Dislocation Configuration Response

Sub-microstructure morphologies in the tensile specimens were also investigated systematically. Figure 7a,d are TEM images of typical dislocation configurations in the dendrite cores at the cross sections that are close to the fracture surface of the DZ406 superalloy at  $-125$  °C. Figure 7a shows that multiple slip bands were observed in the fracture microstructure when tested at  $-125$  °C, and the slip band crossed through several  $\gamma'$  precipitates. A large number of dislocations had been produced in the microstructure, most of them were packed in the  $\gamma$  channel, and some dislocations had been cut in the  $\gamma'$  precipitates (Figure 7d).

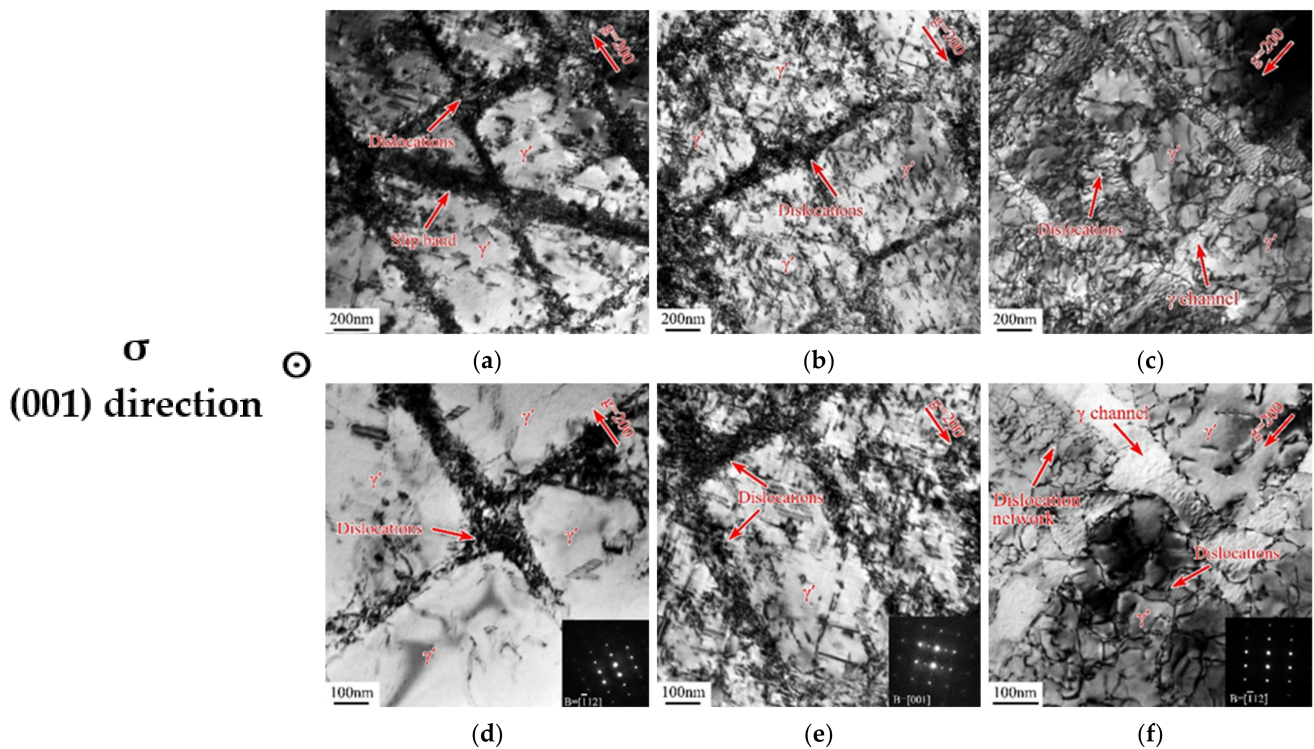


**Figure 7.** TEM images of typical dislocation configurations in the dendrite cores at the cross sections close to the fracture surface of DZ406 superalloy at a lower and higher magnification when tested at  $-125\text{ }^{\circ}\text{C}$  (a,d),  $25\text{ }^{\circ}\text{C}$  (b,e) and  $1000\text{ }^{\circ}\text{C}$  (c,f).

Figure 7b,e show the dislocation configurations in the dendrite cores at the cross sections that are close to the fracture surface of the DZ406 superalloy that was tested at room temperature. A large number of dislocations had been cut in the  $\gamma'$  phase. In addition, the width of the stacking fault decreased, indicating the increased stacking fault energy, thus the dislocations were easier to cross-slip. At  $1000\text{ }^{\circ}\text{C}$ , the sub-microstructure morphology changed obviously, the length of dislocation increased significantly and a dislocation network formed at the interface of  $\gamma/\gamma'$  phases; more dislocations had been cut in the  $\gamma'$  precipitates (Figure 7c,f), compared to that at room temperature (Figure 7b,e). The dislocation density in the  $\gamma$  channel decreased significantly, and the dislocations accumulated at the  $\gamma/\gamma'$  interfaces and partially formed the dislocation networks. Different from cryogenic temperatures and room temperature, the  $\gamma'$  phase was cut in the form of dislocations because of its high stacking fault energy at high temperature [23].

The dislocation morphologies indicated that although the plasticity of DZ406 was improved at room temperature compared with that of cryogenic temperature, the dislocation configuration still maintained similar at cryogenic and room temperatures. Most of the dislocations accumulated in the  $\gamma$  channel; part of the deformation was coordinated in the form of slip band, and the behavior of dislocations cutting in the  $\gamma'$  phase was still in the form of extended dislocations.

Compared with the cryogenic temperature and room temperature, the critical shear stress of the sliding system is reduced at  $1000\text{ }^{\circ}\text{C}$  [24]; the tertiary  $\gamma'$  phase in the  $\gamma$  channel dissolved, and the strength of the  $\gamma'$  phase was greatly reduced [11,25], thus the dislocation was easy to start and had no obstruction in the  $\gamma$  channel. At  $1000\text{ }^{\circ}\text{C}$ , the stacking fault energy of the alloy was high [23], which means the dislocation was prone to cut in the secondary  $\gamma'$  phase directly without stacking faults or bypassing the secondary  $\gamma'$  phase through cross-slip, and without causing strain hardening. Therefore, the yield strength and ultimate strength decreased and the elongation rose significantly at  $1000\text{ }^{\circ}\text{C}$  in comparison with cryogenic temperatures and room temperature. The final sub-microscopic structure

was that dislocations were locally accumulated at the  $\gamma/\gamma'$  interfaces, where the dislocation network formed locally, resulting a large number of dislocations cut in the  $\gamma'$  phase after the dislocation density exceeded the critical value.

The final fracture of the alloy at different temperatures was related to carbides, and the cracking of carbides was the main reason. At cryogenic temperatures, the coordinated deformation ability through the dislocation slip was poor, and the stress concentration around the carbides was easy to form and lead to the final failure; at room temperature and 1000 °C, the dislocations were easy to pass through slip, cross-slip and the shear  $\gamma'$  phase. However, the dislocations were also easy to accumulate at the grain boundaries and around the carbides at 1000 °C, thus there was a high-density dislocation cut in locally. It is speculated that more deformation occurred around the carbides and lead to the final cracking of the carbides, as shown in Figure 8.

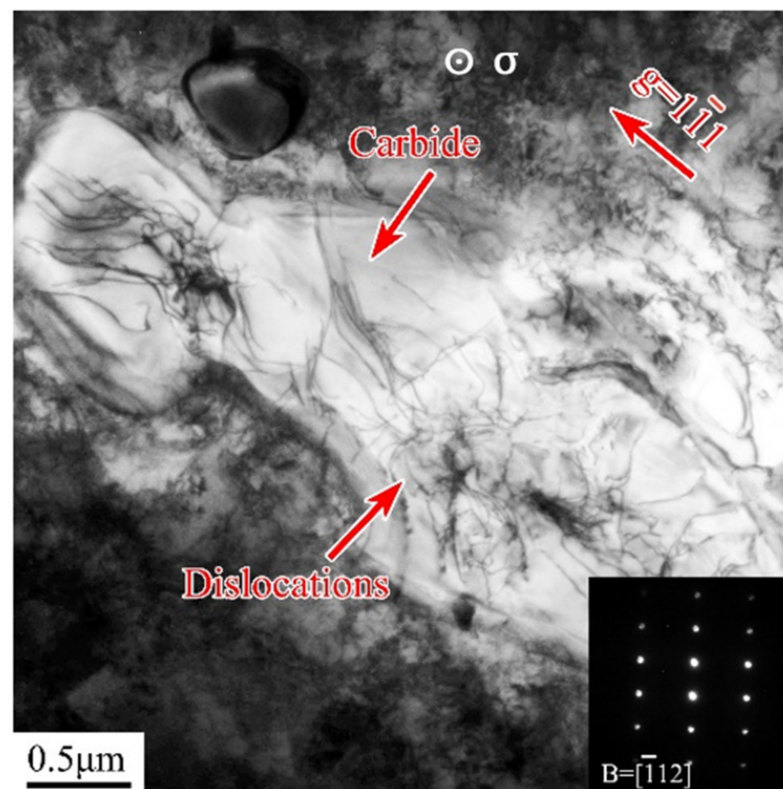


**Figure 8.** TEM images of typical dislocation configurations in the interdendritic region at the cross sections close to the fracture surface of DZ406 superalloy tested at 1000 °C.

In conclusion, the tensile deformation modes of the DZ406 superalloy at cryogenic temperatures and room temperature were significantly different from those at high temperature, which was mainly determined by the changes of stacking fault energy, critical shear stress, phase strength and dislocation configuration with the temperature. The carbides were easy to crack, and because dislocation was easy to move at high temperature, the plastic strain capacity of the material was strong, and the fracture presented a ductile characterization with dimples. Dislocation was difficult to move at cryogenic temperatures, thus accumulating in the  $\gamma$  channel or in the slip bands, and contributing to the deformation during the tensile process. This can be summarized as follows: during the tensile process of the DZ406 superalloy at cryogenic temperatures, the morphologies of the  $\gamma'$  phase and carbides did not change, and they still played an obvious strengthening role, thus the yield strength and ultimate strength of the alloy were still slightly higher than that at room temperature. However, a large number of dislocations and slip bands were also produced at cryogenic temperatures, and a large number of dislocations gathered around the carbides and crack, resulting in an overall elongation of more than 10%.

#### 4. Conclusions

The tensile properties of the directionally solidified superalloy DZ406 were investigated in a large temperature range, and the fractured modes, microstructure characterization, chemical composition and dislocation configuration were systematically investigated. We can draw the following conclusions:

- (1) The yield strength and ultimate strength of the DZ406 superalloy remained around 930 MPa and 1240 MPa in the temperature range from  $-125\text{ }^{\circ}\text{C}$  to  $-25\text{ }^{\circ}\text{C}$ , while they decreased to 910 MPa and 1185 MPa at room temperature, respectively. The elongation remained between 10 and 15% in the temperature range from  $-125\text{ }^{\circ}\text{C}$  to room temperature. At  $1000\text{ }^{\circ}\text{C}$ , the yield strength and ultimate strength decreased to 423 MPa and 581 MPa, while the elongation increased to 25%;
- (2) The DZ406 superalloy suffered brittle fracture and the  $\text{MC}_{(2)}$  carbides cracked during the tensile tests at  $-125$  to  $-25\text{ }^{\circ}\text{C}$ , while ductile fracture and carbides were observed in the middle of the dimples at room temperature and  $1000\text{ }^{\circ}\text{C}$ . The tensile cracks were mainly located in the interdendritic regions at  $-125$  to  $25\text{ }^{\circ}\text{C}$ , they were also found in the grain boundaries at  $1000\text{ }^{\circ}\text{C}$ ;
- (3) The secondary  $\gamma'$  precipitates in the dendrite core regions basically maintained a cuboidal shape and suffered negligible degradation when tested from  $-125\text{ }^{\circ}\text{C}$  to  $1000\text{ }^{\circ}\text{C}$ . The  $\gamma$  phase was rich in Co, Cr and Re, and the  $\gamma'$  phase was rich in Ni, Al, W and Ta. The chemical compositions of the  $\gamma$  phase and  $\gamma'$  phases, as well as the element segregation between the  $\gamma/\gamma'$  phases were close at different testing temperatures from  $-125\text{ }^{\circ}\text{C}$  to  $1000\text{ }^{\circ}\text{C}$ ;
- (4) In the temperature range of  $-125\text{ }^{\circ}\text{C}$  to  $25\text{ }^{\circ}\text{C}$ , most of the dislocations accumulated in the  $\gamma$  channel, and the extended dislocations cut in the  $\gamma'$  phase. In addition, several slip bands crossing the  $\gamma$  channel and  $\gamma'$  precipitates were also observed. At  $1000\text{ }^{\circ}\text{C}$ , dislocations were locally accumulated at the  $\gamma/\gamma'$  interfaces, as well as the dislocation networks, and a large number of dislocations cut in the  $\gamma'$  precipitates.

**Author Contributions:** Experiment—Y.N., G.W. and Z.L.; data and image processing—X.G. and X.Y.; writing—original draft preparation, X.G.; writing—review and editing, H.P. and Z.F. All authors have read and agreed to the published version of the manuscript.

**Funding:** This research is funded by the Science and Technology Program of Guangzhou of China (Grant No. 202102020474), and the CEPREI Innovation and Development Foundation (Grant No. 20Z33 and 20Z32).

**Institutional Review Board Statement:** Not applicable.

**Informed Consent Statement:** Not applicable.

**Data Availability Statement:** Not applicable.

**Conflicts of Interest:** The authors declare that the research was conducted in the absence of any commercial or financial relationships that could be construed as a potential conflict of interest.

#### References

1. Pollock, T.M.; Tin, S. Nickel-based superalloys for advanced turbine engines: Chemistry, microstructure and properties. *J. Propuls. Power* **2006**, *22*, 361. [[CrossRef](#)]
2. Watson, J.E. *Control of Microstructures by Heat Treatments and High-Temperature Properties in High-Tungsten Cobalt-Base Superalloys, in Superalloys: Production, Properties and Applications*; Nova Science Publishers Inc.: New York, NY, USA, 2011.
3. Academic Committee of the Superalloys CSM. *China Superalloys Handbook*; China Zhijian Publishing House: Beijing, China, 2012.
4. Donachie, M.J.; Donachie, S.J. *Superalloys: A Technical Guide*; ASM International: Materials Park, OH, USA, 2002.
5. Reed, R.C. *The Superalloys: Fundamentals and Applications*; Cambridge University Press: New York, NY, USA, 2008.
6. Cervellon, A.; Hémerly, S.; Kürsteiner, P.; Gault, B.; Kontis, P.; Cormier, J. Crack initiation mechanisms during very high cycle fatigue of Ni-based single crystal superalloys at high temperature. *Acta Mater.* **2020**, *188*, 131–144. [[CrossRef](#)]
7. Meid, C.; Eggeler, M. Stress-induced formation of TCP phases during high temperature low cycle fatigue loading of the single-crystal Ni-base superalloy. *Acta Mater.* **2019**, *168*, 343. [[CrossRef](#)]

8. Antonov, S.; Isheim, D. Phosphorous behavior and its effect on secondary phase formation in high refractory content powder-processed Ni-based superalloys. *Materialia* **2019**, *7*, 100423. [[CrossRef](#)]
9. Guo, X.T.; Xing, W.J. Effect of service-induced degradation on residual stress rupture life of a directionally solidified superalloy. *Crystals* **2021**, *12*, 267. [[CrossRef](#)]
10. Guo, X.T.; Liang, Z.S. Effect of overheating temperature on thermal cycling creep properties of K465 superalloy. *Crystals* **2021**, *11*, 1458. [[CrossRef](#)]
11. An, W.; Utada, S. Thermal cycling creep properties of a directionally solidified superalloy DZ125. *J. Mater. Sci. Technol.* **2022**, *104*, 269–284. [[CrossRef](#)]
12. Jaladurgam, N.R.; Kabra, S. Macro- and micro-mechanical behavior of a  $\gamma'$  strengthened Ni-based superalloy at cryogenic temperatures. *Mater. Des.* **2021**, *209*, 109954. [[CrossRef](#)]
13. Nordström, J.; Siriki, R. TWIP and fracture behavior in the superalloy 625 at room and cryogenic temperatures. *Procedia Struct. Integr.* **2019**, *23*, 457–462. [[CrossRef](#)]
14. Ding, Q.; Bei, H. Nano-twin-induced exceptionally superior cryogenic mechanical properties of a Ni-based GH3536 (Hastelloy X) superalloy. *Mater. Today Nano* **2021**, *14*, 100110. [[CrossRef](#)]
15. Xing, W.; Zhu, G. Abnormal creep property degradation in a directionally solidified superalloy DZ406 after suffering overheating. *Mater. Charact.* **2021**, *173*, 110910. [[CrossRef](#)]
16. Hu, G.; Cai, X. *Fundamentals of Materials Science*; Shanghai Jiao Tong University Press: Shanghai, China, 2010.
17. Xing, W.; Liu, C. Effect of solution heat treatment on microstructures and stress rupture properties of DZ406 alloy. In Proceedings of the International Conference on Mechanical Engineering and Applied Composite Materials, Beijing, China, 24–25 October 2020; Springer: Berlin/Heidelberg, Germany, 2021; pp. 421–433.
18. Guo, X.; Zheng, W. High temperature creep behavior of a cast polycrystalline nickel-based superalloy K465 under thermal cycling conditions. *Materialia* **2020**, *14*, 100913. [[CrossRef](#)]
19. Amouyal, Y.; Seidman, D.N. The role of hafnium in the formation of misoriented defects in Ni-based superalloys: An atom-probe tomographic study. *Acta Mater.* **2011**, *59*, 3321–3333. [[CrossRef](#)]
20. Wu, X.; Makineni, S.K. On the segregation of Re at dislocations in the  $\gamma'$  phase of Ni-based single crystal superalloys. *Materialia* **2018**, *4*, 109–114. [[CrossRef](#)]
21. Kontis, P.; Li, Z. The effect of chromium and cobalt segregation at dislocations on nickel-based superalloys. *Scripta Mater.* **2018**, *145*, 76–80. [[CrossRef](#)]
22. Guo, X.; Antonov, S. Solidification rate driven microstructural stability and its effect on the creep property of a polycrystalline nickel-based superalloy K465. *Mater. Sci. Eng. A* **2020**, *770*, 138530. [[CrossRef](#)]
23. Hasan, H.; Milkvik, P. Generalised stacking fault energy of Ni-Al and Co-Al-W superalloys: Density-functional theory calculations. *Materialia* **2020**, *9*, 100555. [[CrossRef](#)]
24. Kolbe, M. The high temperature decrease of the critical resolved shear stress in nickel-base superalloys. *Mater. Sci. Eng. A* **2001**, *319–321*, 383–387. [[CrossRef](#)]
25. Wang, X.G.; Liu, J.L. Tensile behaviors and deformation mechanisms of a nickel-base single crystal superalloy at different temperatures. *Mater. Sci. Eng. A* **2014**, *598*, 154–161. [[CrossRef](#)]